7-2013

# Carbon Nanotube Arrays for Enhanced Thermal Interfaces to Thermoelectric Modules

Kimberly Saviers
*Birck Nanotechnology Center, Purdue University*, ksaviers@purdue.edu

Stephen L. Hodson
*Birck Nanotechnology Center, Purdue University*, slhodson@purdue.edu

Timothy S. Fisher
*Birck Nanotechnology Center, Purdue University*, tsfisher@purdue.edu

James R. Salvador
*Gen Motors Res & Dev Ctr*

Linda S. Kasten
*United States Air Force Research Lab*

JOURNAL OF THERMOPHYSICS AND HEAT TRANSFER
Vol. 27, No. 3, July–September 2013

# Carbon Nanotube Arrays for Enhanced Thermal Interfaces to Thermoelectric Modules

Kimberly R. Saviers,* Stephen L. Hodson,† and Timothy S. Fisher**
Purdue University, West Lafayette, Indiana 47907
James R. Salvador‡
General Motors Research and Development Center, Warren, Michigan 48090
and
Linda S. Kasten§,¶
U.S. Air Force Research Laboratory, Wright–Patterson Air Force Base, Ohio 45433

DOI: 10.2514/1.T4026

**Thermoelectric materials exploit the Seebeck effect in which an electric potential is generated from a supplied temperature gradient. High thermal conductance through the interfaces between the thermoelectric module and its heat source and sink is crucial for generating maximum power. Primarily due to increased surface contact area and inherently low diffusive thermal resistance, carbon nanotube arrays can provide low thermal interface resistance. Vertically aligned carbon nanotube arrays are synthesized on one or both sides of copper foil by microwave plasma chemical vapor deposition. Growth of similar structures on graphitic foil resulted in carbon nanofiber arrays. The products become insertable thermal interface materials. The thermal interface materials are evaluated by measuring the efficiency of a standard bismuth-telluride thermoelectric module with the thermal interface materials applied. Experiments indicate that a copper foil coated on both sides with carbon nanotubes increases thermoelectric power generation by 60% relative to the absence of thermal interface materials and by 25% relative to a bare copper foil. Photoacoustic results indicate that the thermal interface resistance decreases due to the presence of a carbon nanotube, reaching a minimum of 17 $\text{mm}^2\,\text{K/W}$ for a double-sided carbon nanotube film on copper foil. However, carbon nanofiber arrays on graphitic foil showed no improvement in thermoelectric performance or decrease in thermal interface resistance.**



## Nomenclature

| | | |
|---|---|---|
| $I$ | = | current, A |
| $\bar{\kappa}_{n,p}$ | = | average thermal conductivity of the $n$- and $p$-type materials, $\text{W/m} \cdot \text{K}$ |
| $n$ | = | number of legs of each $p$-type and $n$-type material |
| $P_{\text{out}}$ | = | electrical power output, W |
| $Q_H$ | = | heat at the hot side of the thermoelectric, W |
| $R_{\text{block-Ag}}$ | = | thermal interface resistance between the copper block and Ag foil, $\text{mm}^2\,\text{K/W}$ |
| $R_{\text{block-CNT-foil}}$ | = | thermal interface resistance between the copper block and substrate foil with carbon nanotubes, $\text{mm}^2\,\text{K/W}$ |
| $R_{\text{block-foil}}$ | = | thermal interface resistance between the copper block and substrate foil, $\text{mm}^2\,\text{K/W}$ |
| $R_{\text{foil}}$ | = | internal thermal resistance of the substrate foil, $\text{mm}^2\,\text{K/W}$ |
| $R_{\text{foil-Ag}}$ | = | thermal interface resistance between the substrate foil and Ag foil, $\text{mm}^2\,\text{K/W}$ |
| $R_{\text{foil-CNT-Ag}}$ | = | thermal interface resistance between the substrate foil with carbon nanotubes and Ag foil, $\text{mm}^2\,\text{K/W}$ |
| $R_{\text{int}}$ | = | internal electrical resistance of the thermoelectric module, Ω |
| $R_{\text{load}}$ | = | electrical load resistance, Ω |
| $S_{n,p}$ | = | Seebeck coefficient for $n$- and $p$-type legs, V/K |
| $T_C$ | = | cold side temperature, K |
| $T_H$ | = | hot side temperature, K |
| $V_{\text{OC}}$ | = | open circuit voltage, V |
| $\Delta T$ | = | temperature gradient across thermoelectric module, K |
| $\gamma$ | = | aspect ratio of thermoelectric legs |
| $\eta$ | = | thermoelectric efficiency |

Presented as Paper 2012-4048 at the 48th AIAA/ASME/SAE/ASEE Joint Propulsion Conference & Exhibit and 10th International Energy Conversion Engineering Conference Proceeding, Atlanta, GA, 30 July–3 August 2012; received 3 September 2012; revision received 7 February 2013; accepted for publication 13 February 2013; published online 29 May 2013. 

*Graduate Research Assistant, Birck Nanotechnology Center, Mechanical Engineering, 1205 West State Street. Student Member AIAA.

†Graduate Research Assistant, Birck Nanotechnology Center, Mechanical Engineering, 1205 West State Street.

**Professor of Mechanical Engineering, Birck Nanotechnology Center, Mechanical Engineering, 1205 West State Street. Member AIAA (Corresponding Author).

‡Senior Researcher, Chemical Sciences and Material Systems Laboratory, 30500 Mound Road.

§Research Scientist, Thermal Sciences and Materials Branch, Materials and Manufacturing Directorate, 2941 Hobson Way.

¶Research Scientist, Nonstructural Materials Division, 300 College Park; currently Research Scientist, University of Dayton, Dayton, Ohio 45469.

## I. Introduction

IN 2010, 56% of the energy generated in the United States was rejected, most of which was in the form of waste heat resulting from powerplant and vehicle operations, totaling to over 54 quadrillion British thermal units wasted.†† Thermoelectric (TE) modules can convert a portion of this unused heat into usable electricity. These modules operate on the fundamental principle of the Seebeck effect in which a temperature gradient generates electrical power. When united together with any system that expels waste heat, these modules are a clean energy source in that they generate electricity by using no additional natural resources. In much recent research, the TE community has focused on increasing the ZT figure of merit [1–4]; however, system-level optimization is also

††Department of Energy and Lawrence Livermore National Laboratory, "Estimated Energy Use in 2010," URL: https://flowcharts.llnl.gov [retrieved 22 April 2012].

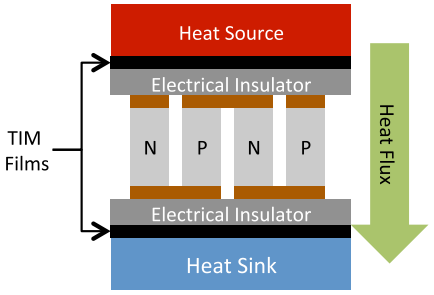


**Fig. 1 Diagram of TE module with nanostructured TIMs.**

required for practical use of TE modules. In particular, the model developed by Yazawa and Shakouri found that the maximum power converted by a TE module is indirectly proportional to the sum of the thermal resistance in the insulating materials around the TE functional material and the thermal resistance external to the module, including the thermal interface resistance [5]. Similarly, but the TE refrigeration modules, Pettes et al. predicted that with a tenfold decrease in contact conductance of the interconnects, peak heat removal capability of the device suffers by at least 10% [6]. The importance of appropriate interfacial thermal and electrical resistance is addressed in the TE review paper by Zebarjadi et al. [7]. The current work focuses on decreasing the thermal interface resistance between the TE module and the opposing heat source or heat sink to harvest waste heat most efficiently.

Thermal interface materials (TIMs) are used to increase thermal conductance across the interface between two materials and conventionally include solders, greases, thermal pads, thermal pastes, and phase change materials. However, recent research has elucidated the potential for vertically aligned carbon nanotube (CNT) arrays synthesized on an insertable substrate to reduce thermal interface resistance. An insertable CNT TIM has the benefit of ease of use in industry. It effectively adds an additional interface; however the performance of the CNT array is such that the thermal transport is enhanced enough to compensate for and provide additional enhancement above the thermal resistance due to the added interface. Much of the research conducted thus far has focused on CNT TIM applications in electronic packaging to enhance cooling; however, these materials could benefit TE operation as well.

Here we include a brief literature review of the thermal interface resistance with basic CNT arrays and insertable nanostructured TIMs: works most relevant to the current application. However, for more detailed instruction on CNTs and thermal transport therein, interested readers should consult [8,9]. Thermal interface resistance values reported for one-sided dry CNT arrays in contact with an opposing surface are 8 [10], 16 [11], 20 [12], and 24 $mm^2$ K/W [13]. The thermal interface resistance of a double-sided CNT film on copper foil is reported to be 10 [14], 12 [15], and 14 $mm^2$ K/W [16], whereas the resistance of a double-sided CNT film on gadolinium foil is reported to be 65 $mm^2$ K/W [17]. In this work the resistance of the double-sided CNT film was measured to be 17 $mm^2$ K/W at 276 kPa, which compares well with similar prior results.

Several innovative techniques have been adopted to decrease these numbers further; these approaches typically involve additive materials that are not stable at elevated temperatures and thus would not be successful in this application. Xu and Fisher used a combination of CNT array and phase change materials to produce a resistance of 5 $mm^2$ K/W [12], Hodson et al. used a palladium thiolate bonding configuration to produce a resistance of 11 $mm^2$ K/W [18], Panzer et al. deposited a layer of palladium on top of the CNT array to produce a resistance of 12 $mm^2$ K/W [19], and Ngo et al. used a copper gap filler with vertically aligned carbon nanofibers (CNFs) for a resistance of 25 $mm^2$ K/W [20]. This list is not exhaustive; many inventive configurations that include vertically aligned CNTs and CNFs can be found in [9,21–23], and throughout the literature. Note that these thermal interface resistance values may not be directly comparable because they differ in substrate materials, contacting surface materials and properties, and measurement techniques. Current techniques include the steady-state one-dimensional reference bar, laser flash, photoacoustic, $3\omega$, thermoreflectance, and infrared microscopy [24].

The thermal conductivity of a single multiwall carbon nanotube (MWCNT) has been measured in the expansive range of 42–3000 W/mK; however, because many MWCNTs act in parallel in an array configuration, the effective conductivity decreases to 12–83 W/mK according to measured values in the literature [25]. For a polymer nanocomposite consisting of vertically aligned CNTs that have been mechanically densified Marconnet et al. reported an effective conductivity up to 4.87 W/mK [9]. The thermal enhancement that results from the application of CNT arrays appears to be primarily due to increased surface contact area [26]. Inherent roughness in the opposing surfaces creates microscale gaps that inhibit phonons from traveling across an interface; however, vertically oriented CNTs serve to bridge that gap. With a CNT TIM in place, the dominant thermal resistance lies at the interface between the opposing surface and the CNT free tips [11]. The thermal performance of CNT arrays can depend on factors such as CNT height, diameter, quality, structure, and chirality; as well as array density, coverage and morphology. Increased control over these factors will be essential for industrial use.

A unique challenge exists for TIMs in TE applications because the operating environment is commonly extreme with high temperatures, corrosive gases, high- and low- frequency vibration, and thermal shock. In vehicle exhaust and power plant applications, TE operation temperatures may be near 600°C and 2000°C, respectively. Amorphous CNTs decompose due to oxidation near 300°C, but increased thermal stability has been achieved [27]. Another important characteristic of an effective TIM, specifically for a TE module, includes mechanical compliance to accommodate the significant coefficient of thermal expansion (CTE) mismatch of the materials on either side of the interface. Thus, the low shear modulus of CNT arrays is ideal [28]. CNTs are known to exhibit remarkably high Young's moduli in the axial direction on the order of 1 TPa [29], making them very stiff. They also have high resilience, readily returning back to the original shape after a load is released [30]. Mechanical testing via a laser Doppler method showed that the in-plane modulus of a vertically aligned CNT array on polysilicon is relatively low, in the range of 8 to 300 MPa, for CNT heights of 0.5 to 100 $\mu$m [31]. To address the internal interfaces to a TE module, Gao et al. demonstrated that CNT synthesis is possible on SiGe, a thermoelectric material, and reported thermal resistances from 1.4 to 4.3 $mm^2$ K/W [28]. This work may be complemented by the present work to address the possibility of CNT array films at the external interfaces of the TE module as shown in Fig. 1.

CNT array films fabricated on copper foil and CNFs fabricated on graphitic foil are evaluated here using two techniques. In the first technique, the power output and efficiency of a standard bismuth telluride ($Bi_2Te_3$) TE module are measured with a CNT array TIM in place on the hot side of the module. These functional performance results are complemented with photoacoustic (PA) thermal conductance experiments to quantify the thermal resistance at the interface.

## II. Experimental Techniques

### A. Fabrication of Samples

The substrate materials chosen for evaluation are copper foil of 100 $\mu$m thickness (Alfa Aesar Puratronic, 99.9999% metals basis) and graphitic foil of 130 $\mu$m thickness (GrafTech International GRAFOIL® GTA, through plane thermal conductivity 5 W/mK). A previously unreported five-layer catalyst system was used on all samples consisting of 10 nm Ti, 100 nm Ni, 30 nm Ti, 10 nm Al, and 5 nm Fe in order from the metal layer directly on the substrate to the outside catalyst metal layer. The first Ti layer promotes adhesion to the substrate and the Ni layer inhibits interdiffusion of Fe catalyst particles into underlying layers. The remaining three layers are well-known catalyst supports for vertically aligned multiwalled carbon nanotube (MWCNT) arrays. The Al layer promotes nucleation of CNTs by segregating Fe particles during the annealing step of the microwave plasma chemical vapor deposition (MPCVD) process.

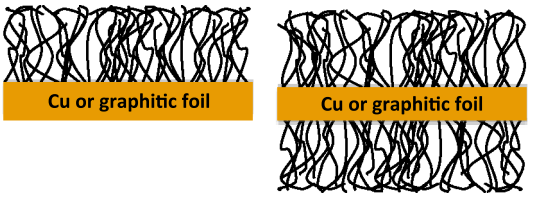


**Fig. 2 Schematic of single-sided and double-sided insertable CNT or CNF TIMs.**

More uniform CNT coverage was found when thermal vapor deposition was employed in comparison to electron beam deposition; therefore, the catalyst stack on each substrate was deposited by thermal vapor deposition.

Arrays of MWCNTs were synthesized using a SEKI AX5200S microwave plasma vapor deposition system in which methane serves as the carbon source to synthesize the CNTs [32,33]. On copper foil, the MPCVD process was the following: the substrate was heated to 800°C while annealing in $N_2$, followed by CNT synthesis for 2 min in $H_2$ and $CH_4$ at a plasma generator power setting of 300 W. For the graphitic foil, the substrate was heated to 600°C while annealing in $N_2$ followed by synthesis for 3 min in $N_2$, $H_2$, and $CH_4$ at a plasma generator power setting of 300 W. Double-sided samples were synthesized by subsequently following the same procedure on the second side. It has been observed that CNF array growth on the graphitic foil is macroscopically more uniform when $N_2$ is present. We theorize that the $N_2$ causes defects in the graphitic substrate, aiding in nucleation of the carbon ions. Also, the presence of $N_2$ aids in producing more ions in the plasma, affecting the plasma coupling with the substrate. A schematic of the resulting structure is shown in Fig. 2.

### B. Characterization of Samples

All samples were imaged using a Hitachi S-4800 field emission scanning electron microscope (FESEM). Compared to CNF arrays on graphitic foil, the CNT arrays on copper foil are shorter, denser, more vertically oriented, exhibit more uniform height, and are much less entangled. These characteristics can be observed in representative images of the arrays shown in Fig. 3. An approximate volume fraction of each nanoarray was obtained by weighing the sample before and after synthesis, measuring the effective array coverage area from a low magnification FESEM image, and determining the approximate average height with FESEM imaging. The CNT arrays on both the single-sided and double-sided copper foil films had an approximate height of 10 $\mu$m and volume fraction of 4.5%. By estimating the density of a single tube to be that of graphite (2060 kg/m$^3$), the effective density of the CNT array is approximately 93 kg/m$^3$. CNF arrays on graphitic foil were approximately 35-$\mu$m-long with a volume fraction of 1.2% and density of approximately 24 kg/m$^3$.

A Titan environmental transmission electron microscope (TEM) imaged a sample of each type. The nanostructures were scraped from their substrates and dispersed by sonication in acetone. From the images displayed in Fig. 4 the nanostructures on copper foil are clearly CNTs, whereas the nanostructures on graphitic foil are CNFs. The CNTs have diameter of approximately 6 nm with 15 walls. The CNFs are significantly larger at 30 nm with a cone-shaped structure. Areas of the CNFs are hollow in the center, whereas other areas appear to have amorphous carbon in the center.

Raman spectroscopic measurements were performed by using 532 nm laser excitation, revealing that the CNFs contain comparatively less defects with a $I_D/I_G$ intensity ratio of 0.14, whereas the CNTs were much more defective with a $I_D/I_G$ intensity ratio of 1.6. As mentioned earlier, $N_2$ was fed in the MPCVD system during synthesis of CNFs. Therefore, the plasma characteristics (plasma temperature and constituents) might be different from that of CNT growth, for which $N_2$ was not fed into the plasma. Introduction of $N_2$ into the MPCVD plasma is well known to increase the graphitic crystallinity in carbon films due to enhanced $sp^2$ carbon content [34,35].

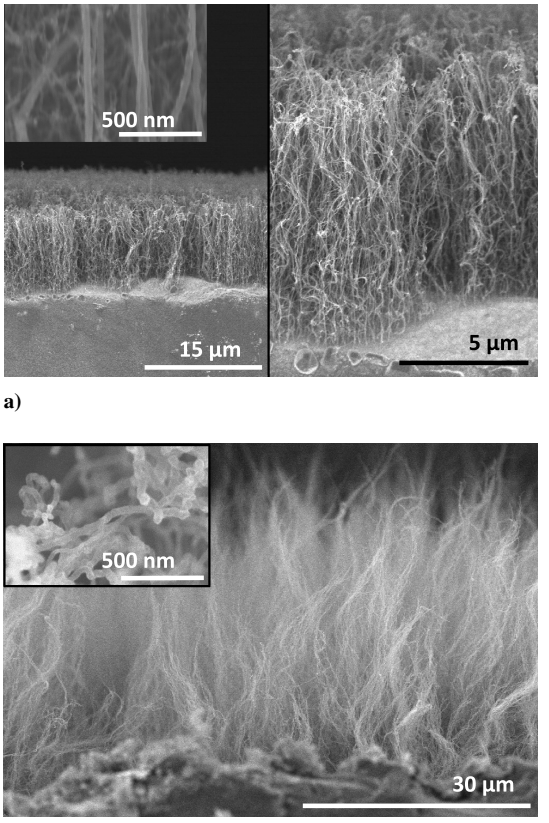


**Fig. 3 Representative FESEM images of samples: a) CNT array on copper foil and b) CNF array on graphitic foil.**

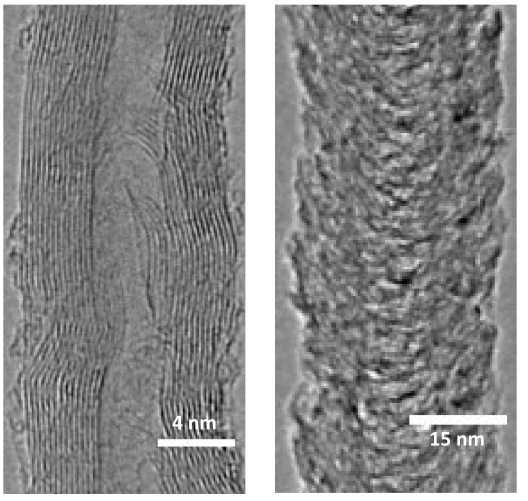


**Fig. 4 TEM images of a) CNT on copper foil and b) CNF on graphitic foil.**

It was previously theorized that TiC forms at the substrate during synthesis, which is in direct contact with CNTs in the final configuration [36]. The formation of TiC leads to a strong thermal connection between the substrate and the CNTs, and thus a low resistance. The presence of TiC in CNTs is confirmed here by time-of-flight secondary ion mass spectrometry (TOF-SIMS). The TOF-SIMS analysis measurements were performed using an IONTOF TOF-SIMS.5 (IONTOF Gmbh, Münster, Germany) mass spectrometer equipped with a bismuth liquid metal ion gun. Spectra were acquired in the positive secondary ion polarity using a high mass resolution setting and the following conditions: 1) primary ion: $Bi_1^+$, 25 kV; 2) primary ion current: 0.9 pA; 3) analysis area: 50 × 50 $\mu$m$^2$;

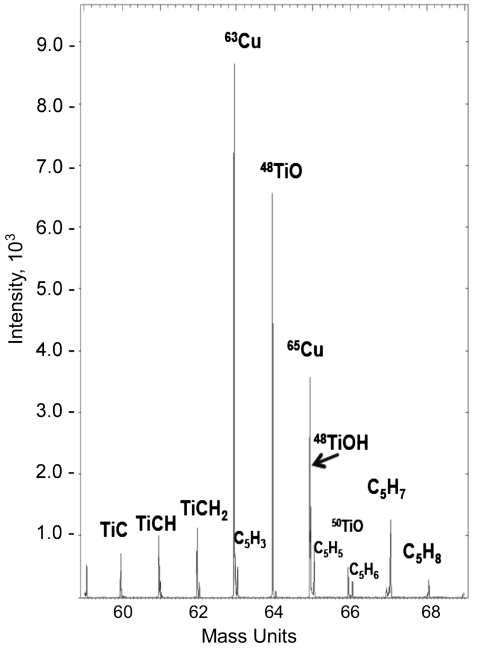


**Fig. 5 TOF-SIMS results of CNTs on copper foil.**

and 4) acquisition time: 20 s. In the analysis, a pulsed primary ion beam focused on the substrate bombards the surface, causing ion collision processes to occur. Some collisions return to the surface and result in the emission of ionized atoms and atom clusters. By using a very low primary ion flux density, no point on the surface is struck more than once by a primary particle and thus, the surface is said to be static. The information obtained is characteristic of the chemistry of the surface layer. These secondary ions are accelerated into a time-of-flight mass spectrometer where they are mass analyzed by measuring their time of flight from the sample surface to the detector. The highly resolved masses are used to determine the composition at the surface [37]. The resulting analysis is shown in Fig. 5, which shows a clear presence of TiC and derivatives. The oxides present are a result of oxidation that occurred after synthesis.

Films made for TE efficiency testing were square of area 4 $cm^2$, whereas samples made for PA testing were square of area 1 $cm^2$. Equivalent samples were fabricated for each testing method at the same synthesis parameters. Although not observed in this study, we note that the sample size may affect the resulting nanostructures; however, it is appropriate to compare the films within each testing method.

### C. Thermoelectric Efficiency Testing

An off-the-shelf TE cooling module composed of $Bi_2Te_3$ materials and with dimensions 2 cm × 2 cm × 0.4 cm was used for all measurements (Marlow Industries RC3-6-01S). TE energy conversion measurements were performed using a commercially available ULVAC PEM-2 module efficiency measurement system, shown in Fig. 6. The measurement was performed by establishing a temperature gradient across the TE module via steady-state heat flow. The module is connected to power electronics that supply a continuously variable load resistance, allowing a current vs voltage curve to be generated at each of the predetermined temperature gradients. All measurements were performed under dynamic vacuum to reduce convective heat loss and to ensure module health. The TIMs under investigation were inserted between the heat source and the hot side of the module. The interface material between the cold side of the module and the heat sink was bare graphitic foil for all measurements.

The heat flow into the module was monitored through the heat source by measuring the temperature drop along its length through a series of three thermocouples. The heat source is a Ni block with a cross-sectional area equal to that of the modules. Nonlinearity in the temperature profile is attributed to radiative loss at the exposed surfaces of the block, but was not corrected for in the measurements, as it was assumed to be a common value to all measurements performed. On the cold side of the module is a symmetrically disposed copper block heat sink with an identical cross section, which was used to monitor heat flow rejected from the module by the same method. The cold block was cooled by an external chiller loop set to 20.0°C. Thermocouples are embedded into the heat source and sink blocks in close proximity (1 mm) to the ceramic headers on the hot side and cold side of the module and were used to transduce the temperatures, which provide a measure of the temperature gradient across the module. Transport property data for the TE materials that comprise the module were supplied by Marlow Industries and include the temperature dependence of the Seebeck coefficient, electrical resistivity, and the thermal conductivity.

Polynomial fits to the temperature dependence of these parameters were used in subsequent analysis of the TE module performance. Magnitude and temperature dependence of the Seebeck coefficient is used to estimate the open circuit voltage ($V_{OC}$) of the module using the relationship

$$V_{OC} = \int_{T_c}^{T_H} S_p(T) \cdot n \, dT - \int_{T_c}^{T_H} S_n(T) \cdot n \, dT \tag{1}$$

where $S_p(T)$ and $S_n(T)$ are the temperature dependence of the Seebeck coefficients for the $n$- and $p$-type materials, respectively; $n$ is the number of legs of each type of material that comprise the module, and $T_C$ and $T_H$ are the cold and hot side temperatures of the legs in the module. Note that due to the thermal contact resistance and the thermal resistance of the ceramic header, the temperature differential across the legs will be smaller than that of the module as a whole.

Polynomial fits to the thermal conductivity allow a comparison of the heat flow measured to that predicted for the module. However, it was found that due to the large magnitude of the internal electrical contact resistance found in these modules, the electrical resistivity data for the materials offered little insight into the module behavior. Instead, the internal electrical resistance of the modules $R_{int}$ at each temperature gradient was measured by taking the slope of the I-V curve. With the data provided by Eq. (1), the electrical power output as a function of the externally applied load resistance $R_{load}$ was calculated by

$$P_{out} = V_{OC}^2 \left( \frac{R_{load}}{(R_{int} + R_{load})^2} \right) \tag{2}$$

Neglecting subtle effects such as the Thompson coefficient, the maximum power output occurs at the condition $R_{load} = R_{int}$. The conversion efficiency $\eta$ is simply the quotient of the electrical power output $P_{out}$ and the heat delivered to the hot side of the module $Q_H$, which is the sum of the steady-state heat flow due to the temperature differential including Peltier and Joule terms. If we assume that the

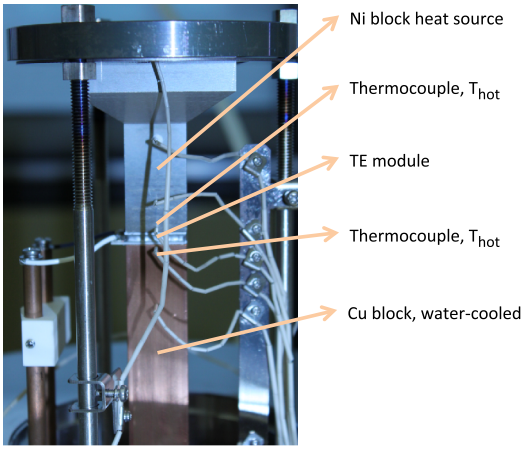


**Fig. 6 Apparatus for evaluation of TIMs using a TE module. Vacuum chamber not shown.**

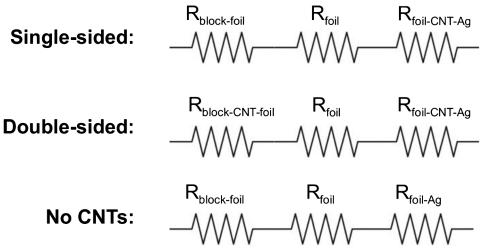


**Fig. 7 Equivalent thermal resistance networks resolved for samples. Here CNT can refer to the CNT array or the CNF array.**

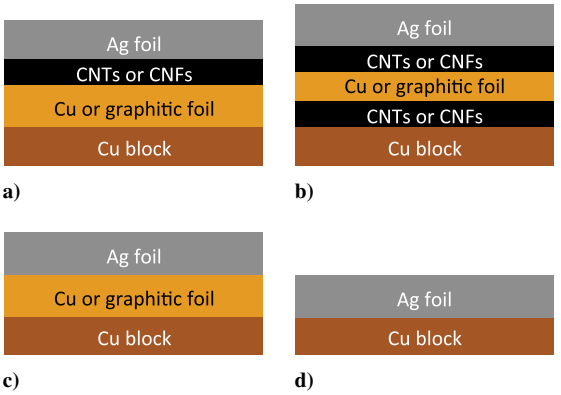


**Fig. 8 Configurations used in the PA testing: a) single-sided, b) double-sided, c) bare, and d) no sample.**

Joule heating within the TE modules is symmetrically disposed at the hot and the cold side of the junction, $Q_H$ can be expressed simply as

$$Q_H = \bar{\kappa}_{n,p} \cdot \gamma \cdot \Delta T \cdot 2n + (S_{n,p} \cdot I \cdot T_H) - \frac{1}{2} \cdot I^2 \cdot R_{\text{int}} \quad (3)$$

where $\bar{\kappa}_{n,p}$ is the average thermal conductivity of the $n$- and $p$-type materials, $\gamma$ is their geometrical aspect ratio, $\Delta T$ is the temperature gradient, $S_{n,p}$ is the magnitude of the Seebeck coefficient of the $n$- and $p$-type materials at $T_H$, $I$ is the current flowing in the module, and $2n$ is the total number of $n$- and $p$-type legs in the module. Each thermal interface material was investigated at four different temperature gradients. In the interest of clarity, only the largest temperature gradient results, where the benefit of the TIMs is most demonstrable, are presented.

### D. Photoacoustic Technique

In support of the application-oriented TE testing, the thermal interface resistance of the CNT arrays was measured by the PA technique, which has been thoroughly documented by Hu et al. [38] and by Cola et al. [11]. Following these works, a brief description of the method is included here. The sample in question, consisting of any number of layers of material, is below a small cell that is pressurized with He. The surface opposing the CNT array is 25-$\mu$m-thick silver foil. An o-ring lies upon the sample to create a gas-tight seal to the cell. A microphone is embedded into the cell, situated properly to measure the acoustic signal emitted from the contents of the cell. A modulated laser beam is focused onto the surface of the sample, inducing a temperature gradient in the sample. Heat is absorbed by a thin 80 nm Ti layer, which coats the silver foil. Heating of the sample causes a change in temperature in the gas layer and ultimately a change in pressure. This periodic change in pressure results in an acoustic signal that is recorded by the embedded microphone and resolved into amplitude and phase measurements. One-dimensional heat conduction relations in the sample layers and thermodynamic relations in the gas layer govern the system. A nonlinear least-squares regression is then used to resolve the interface resistances between layers in the sample. A representation of the thermal network is shown in Fig. 7, along with the sample configurations that were tested with the PA technique in Fig. 8. All resistances were determined for the respective single- and double-sided samples.

In a given measurement, uncertainty can arise from the phase shift and estimation of parameters such as the density and height of the nanoarray. The uncertainty associated with measurement of the phase shift of the reference sample (80 nm Ti on quartz) is much greater than that of the sample with the nanoarray and silver foil due to the fact that multi-layer samples exhibiting higher total resistances consequently produce more stable signals. The phase shift of the reference sample can vary $\pm 1.0°$ whereas the nanostructured sample only varies by $\pm 0.2°$. Therefore, the experimental uncertainty is dominated by the phase shift of the reference sample. The uncertainty corresponding to the nonlinear regression fit of the interface resistance and estimation of the nanoarray density and height fall within the uncertainty produced by the phase shift of the reference sample. Hence, the total uncertainty is estimated by shifting the phase shift of the reference sample by $\pm 1.0°$.

## III. Results and Discussion

Two techniques were used to evaluate the influence of CNT-based TIMs on thermal interface resistance. In the first technique, the TIMs were applied to a TE module, and the resulting efficiency was resolved. This technique was aimed to mimic a system-level scenario. The TE efficiency testing was performed at a loading pressure of 2.45 MPa with the interface material placed on the hot side of the TE module. In the case of the single-sided CNT TIMs, the CNT array was oriented toward the nickel heat source. The temperature difference across the module in each test was 95°C; the hot side temperature was 120°C and the cold side temperature was 25°C.

Current-voltage curves were generated with each TIM in place and are displayed in Fig. 9. The slope of all the curves are approximately equal, indicating that the internal resistance of the modules was not affected significantly by the differing TIMs, due largely to the rather weak temperature dependence of the resistivity of the TE materials and module. There is a steady increase in $V_{\text{OC}}$ when transitioning from a graphitic foil TIM to copper and finally to the single- and double-sided CNT arrays, which produce the highest $V_{\text{OC}}$ for the module. We conclude that the higher $V_{\text{OC}}$ observed when CNT TIMs were used is due to the decrease in the thermal contact resistance between the heat source and the TE module, leading to a higher temperature gradient across the TE functional material.

As indicated previously, $V_{\text{OC}}$ is a function of the magnitude and temperature dependence of the Seebeck coefficient. To estimate the $V_{\text{OC}}$ for the module, Eq. (1) was used in conjunction with both the polynomial fit to the Seebeck coefficients of the $n$- and $p$-type materials and the temperatures measured at the bottom of the hot source and the top of the heat sink. The theoretical $V_{\text{OC}}$ for the module used in this study is approximately 1.22 V. For the double-sided CNT TIM, the $V_{\text{OC}}$ approaches this value. Because CNT arrays are used only at the hot side junction, we expect that the $V_{\text{OC}}$ for the module will remain below the calculated value as the cold side junction remains a significant source of thermal contact resistance. The increase in the efficiency of the module can therefore be attributed to the increase in electrical power output with only small changes in the heat flux into the module with different TIMs. As evident from Eq. (2), decreases in the $V_{\text{OC}}$ as a result of thermal contact resistance degrade power output for the modules as this resistance represents a significant source of thermal parasitic loss at the system level.

The measured efficiency as a function of output current for various interface conditions is shown in Fig. 10. Relative to a condition in which no TIM is applied, the maximum TE efficiency increases by 35% when a single-sided CNT copper film is applied and by 60% when a double-sided film is applied. Furthermore, relative to a bare copper foil, the addition of CNTs to one and both sides of the foil increases the maximum efficiency by 10% and 25%, respectively, indicating that the presence of vertically oriented CNTs on copper foil has a significantly positive influence on TE module performance.

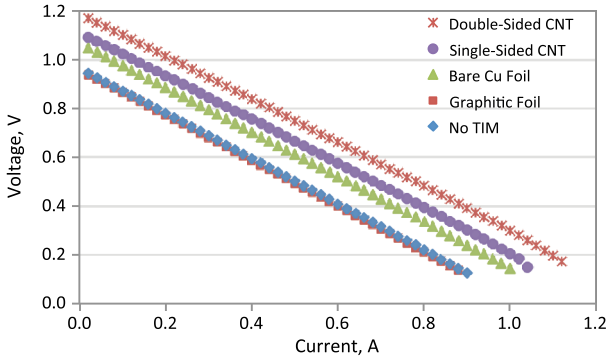


**Fig. 9 I-V curve for a TE module with various TIMs. Graphitic foil and no TIM data overlap.**

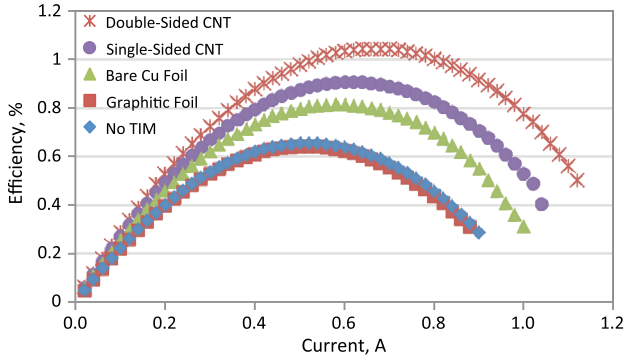


**Fig. 10 TE efficiency for a TE module with various TIMs.**

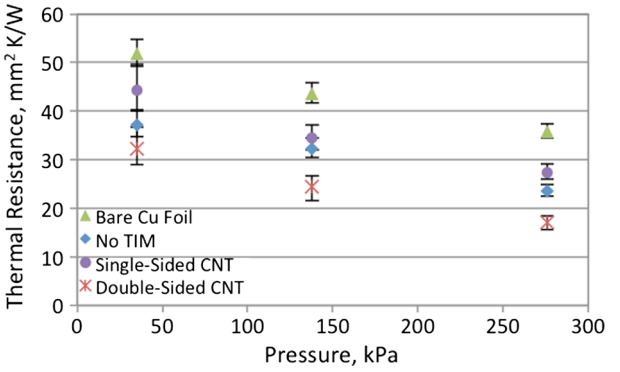


**Fig. 11 Thermal interface resistance at various pressures resolved with the PA technique.**

CNF arrays on graphitic foil were also measured with this technique, however, no positive influence on TE performance was observed.

The high pressure (2.45 MPa) during the test is likely to cause buckling of the CNTs. Maschmann et al. used a digital image correlation analysis to show that the deformation modes of a CNT array include bending, crushing, and bottom-up buckle accumulation [39]. Lin et al. found a 70% decrease in thermal conductivity due to the breakdown of the outer shell of MWCNTs as a result of buckling [25]. In the current study, buckling was observed via FESEM imaging of nanostructures under axial load and after the high pressure testing. However, buckling of some CNTs causes more engaged CNTs in contact with the opposing substrate. We maintain that the dominating factor in our measurement is the contact area of the nanostructures on the opposing substrate.

The thermal contact resistance values were measured using the PA technique to provide a basis of comparison with the previous results. The contact resistance of each material was evaluated in a configuration where the TIM was pressed against a 25-$\mu$m-thick silver foil at contact pressures of 34, 137, and 276 kPa and at room temperature. Thermal contact resistance as a function of contact pressure using the PA technique is shown in Fig. 11. At a contact pressure of 276 kPa, the thermal interface resistance is 36 mm$^2$ K/W for bare copper foil, 27 mm$^2$ K/W for a single-sided CNT film on copper foil, 24 mm$^2$ K/W for no TIM, and 17 mm$^2$ K/W for a double-sided CNT film on copper foil.

The results show a decrease in thermal resistance due the presence of CNTs compared to the lack of CNTs on copper foil. The resistance values for no TIM are lower than may be expected; however, we attribute the low values attained with no TIM to the nature of the opposing substrate used in the test. The silver foil has very low surface roughness and is much more flexible than a solid surface, leading to an inherently different interface topology. When the silver foil is pressed directly against a solid copper block, the foil may conform to microscopic surface asperities. This effect will lead to a lower thermal interface resistance compared to a configuration in which the silver foil is pressed against a copper foil, another relatively thin and flexible material. Two solid surfaces in contact, as found in most engineering applications, will behave differently. Relative to a bare copper foil, the reduction in contact resistance due to a double-sided CNT TIM is 50% at a contact pressure of 276 kPa, whereas the corresponding increase in TE module efficiency is 25% at a pressure of 2.45 MPa. Because of limitations associated with the microphone used in the PA technique, tests could not be performed at pressures above 276 kPa; however, we expect the contact resistances to decrease further with increasing pressure due to increased engaged area.

The resistance values in this study are approximately 1.5 to 2 times higher than those in a similar PA technique study in [14]. Currently, the reason for the discrepancy is not clear; however, there are important differences between the two studies. The copper substrate thickness in this study is 100 $\mu$m, the CNT height is 10 $\mu$m, and the CNT diameter is 6 nm. In the reference, the corresponding parameters are 10 $\mu$m thickness, 50 $\mu$m height, and 20 nm diameter. The volume fraction was not able to be compared. Because of the effective thermal conductivity and the surface roughness of the opposing substrate, an optimal CNT height exists in each application.

Graphitic foil was also tested with the PA technique, with and without CNFs. The bare graphitic foil caused an interface resistance of 72 mm$^2$ K/W at 276 kPa, and no improvement in performance was observed with the addition of CNFs. CNFs have significantly lower thermal conductivity than CNTs on the order of 10 W/mK [40]. As shown in Fig. 3, the CNF array on graphitic foil is visibly less aligned than the CNT array on copper foil, reinforcing the idea that nanostructure alignment is an important characteristic for creating contact area and reducing contact resistance. A synthesis recipe specific to graphitic materials may be developed in the future to yield CNT arrays on this substrate.

The two measurement techniques used exhibit clear differences; therefore, more than a qualitative comparison of measured data may not be appropriate. In addition to the different contact pressures, the material opposing the CNTs in the PA technique was relatively thin and flexible compared to the opposing surface used in the TE efficiency testing. Despite these differences, both techniques illustrate the beneficial role that the vertically aligned CNT arrays play in reducing thermal contact resistance and thus increasing TE module efficiency.

## IV. Conclusions

The study herein has shown a significant decrease in thermal interface resistance due to the presence of carbon nanotube (CNT) arrays on both sides of copper foil, accompanied by a significant increase in efficiency when applied to the hot side of a standard thermoelectric (TE) module. A film with CNTs on one side of copper foil leads to an increase in efficiency of the TE module, which increases further when a double-sided CNT film is applied. The thermal interface resistance of a copper foil with CNTs on both sides is 17 mm$^2$ K/W, which corresponds to a 60% relative increase in TE module efficiency compared to a condition with no interface material and a 25% relative increase in efficiency compared to a bare copper foil. The thermal interface resistance of the graphitic foil substrate

with carbon nanofiber (CNF) arrays was the highest of all samples tested. However, poor performance was likely because the thermal conductivity of CNFs is relatively low. Also, a qualitative inspection of the field emission scanning electron microscope (FESEM) images reveals nonideal density, alignment, and height uniformity characteristics. The synthesis recipe for graphitic foil may be adjusted to yield CNT arrays that lead to lower thermal interface resistance. The thermal resistance values that were measured in this study were on par with others in the literature, and further optimization of the CNT thermal interface materials (TIMs) could bring the values to a lower level.

The mechanical characteristics of the CNT TIMs may be more suitable for high temperature applications than commercial TIMs. In the future, efficiency testing should be performed with CNT TIMs on both the hot side and cold side of the TE module at moderate pressures. Also, efforts should be taken to understand the behavior of CNT TIMs at elevated temperatures, including interface characterization at temperatures upward of 1000°C with repeated thermal cycling. A limited number of thermal and humidity cycling studies have been performed on conventional TIMs. Increased stability at high temperatures may result from chemically doping the CNT arrays. In the long term, application-oriented studies should be performed to understand the feasibility of incorporating the CNT TIMs into fully engineered systems.



## Acknowledgments

The work is sponsored by the National Science Foundation/U.S. Department of Energy Partnership on Thermoelectric Devices for Vehicle Applications. Support from the U.S. Department of Energy under corporate agreement DE-FC26-04NT42278 to General Motors Corporation is also gratefully acknowledged. Kimberly Saviers appreciatively acknowledges support from the Laura Winkelman Davidson Fellowship for Doctoral Studies at Purdue University. Lastly, the authors thank Rajib Paul for performing Raman spectroscopy characterization and Sammy Saber for performing TEM imaging.

## References

[1] Balandin, A. A., and Lazarenkova, O. L., "Mechanism for Thermoelectric Figure-of-Merit Enhancement in Regimented Quantum Dot Superlattices," *Applied Physics Letters*, Vol. 82, No. 3, 2003, pp. 415–417. doi:10.1063/1.1539905

[2] Fan, Z. Y., Wang, H. Q., and Zheng, J. C., "Searching for the Best Thermoelectrics Through the Optimization of Transport Distribution Function," *Journal of Applied Physics*, Vol. 109, No. 7, 2001, pp. 073713-1–073713-6. doi:10.1063/1.3563097

[3] Lee, J. H., Wu, J. Q., and Grossman, J. C., "Enhancing the Thermoelectric Power Factor with Highly Mismatched Isoelectronic Doping," *Physical Review Letters*, Vol. 104, No. 1, 2010, pp. 016602-1–016602-4. doi:10.1103/PhysRevLett.104.016602

[4] Mahan, G. D., and Sofo, J. O., "The Best Thermoelectric," *Proceedings of the National Academy of Sciences of the United States of America*, Vol. 93, No. 15, 1993, pp. 7436–7439. doi:10.1073/pnas.93.15.7436

[5] Yazawa, K., and Shakouri, A., "Cost-Efficiency Trade-Off and the Design of Thermoelectric Power Generators," *Environmental Science and Technology*, Vol. 45, No. 17, 2011, pp. 7548–7553. doi:10.1021/es2005418

[6] Pettes, A. M., Hodes, M. S., and Goodson, K. E., "Optimized Thermoelectric Refrigeration in the Presence of Thermal Boundary Resistance," *IEEE Transactions on Advanced Packaging*, Vol. 32, No. 2, 2009, pp. 423–430. doi:10.1109/TADVP.2008.924221

[7] Zebarjadi, M., Esfarjani, K., Dresselhaus, M. S., Ren, Z. F., and Chen, G., "Perspectives on Thermoelectrics: From Fundamentals to Device Applications," *Energy and Environmental Science*, Vol. 5, No. 1, 2012, pp. 5147–5162. doi:10.1039/c1ee02497c

[8] Cola, B. A., Fisher, T. S., and Xu, X. F., "Carbon Nanotube Array Thermal Interfaces," *Carbon Nanotubes: New Research*, edited by Ottenhouse, A. P., Nova Science Publishers, New York, 2009, pp. 101–110.

[9] Marconnet, A., Yamamoto, N., Panzer, M., Wardle, B., and Goodson, K., "Thermal Conduction in Aligned CNT-Polymer Nanocomposites with High Packing Density," *ACS Nano*, Vol. 5, No. 6, 2011, pp. 4818–4825. doi:10.1021/nn200847u

[10] Cola, B. A., Xu, X., Fisher, T. S., Capano, M. A., and Amama, P. B., "Carbon Nanotube Array Thermal Interfaces for High-Temperature Silicon Carbide Devices," *Nanoscale and Microscale Thermophysical Engineering*, Vol. 12, No. 3, 2008, pp. 228–237. doi:10.1080/15567260802183015

[11] Cola, B. A., Xu, J., Cheng, C. R., Xu, X. F., Fisher, T. S., and Hu, H. P., "Photoacoustic Characterization of Carbon Nanotube Array Thermal Interfaces," *Journal of Applied Physics*, Vol. 101, No. 5, 2007, pp. 054313-1–054313-9. doi:10.1063/1.2510998

[12] Xu, J., and Fisher, T. S., "Enhancement of Thermal Interface Materials with Carbon Nanotube Arrays," *International Journal of Heat and Mass Transfer*, Vol. 49, Nos. 9–10, 2006, pp. 1658–1666. doi:10.1016/j.ijheatmasstransfer.2005.09.039

[13] Amama, P. B., Lan, C., Cola, B. A., Xu, X., Reifenberger, R. G., and Fisher, T. S., "Electrical and Thermal Interface Conductance of Carbon Nanotubes Grown Under Direct Current Bias Voltage," *Journal of Physical Chemistry C*, Vol. 112, No. 49, 2008, pp. 19727–19733. doi:10.1021/jp807607h

[14] Cola, B. A., Xu, X. F., and Fisher, T. S., "Increased Real Contact in Thermal Interfaces: A Carbon Nanotube/Foil Material," *Applied Physics Letters*, Vol. 90, No. 9, 2007, pp. 093513-1–093513-3. doi:10.1063/1.2644018

[15] Wang, H., Feng, J., Hu, X., and Ng, K. M., "Synthesis of Aligned Carbon Nanotubes on Double-Sided Metallic Substrate by Chemical Vapor Deposition," *Journal of Physical Chemistry C*, Vol. 111, No. 34, 2007, pp. 12617–12624. doi:10.1021/jp0730848

[16] Wang, H., Feng, J. Y., Hu, X. J., and Ng, K. M., "Reducing Thermal Contact Resistance Using a Bilayer Aligned CNT Thermal Interface Material," *Chemical Engineering Science*, Vol. 65, No. 3, 2012, pp. 1101–1108. doi:10.1016/j.ces.2009.09.064

[17] McCarthy, P. T., Marinero, E. E., and Fisher, T. S., "Carbon Nanotube Thermal Interfaces on Gadolinium Foil," *International Journal of Heat and Mass Transfer*, Vol. 55, Nos. 23–24, 2012, pp. 6716–6722. doi:10.1016/j.ijheatmasstransfer.2012.06.080

[18] Hodson, S. L., Bhuvana, T., Cola, B. A., Xu, X. F., Kulkarni, G. U., and Fisher, T. S., "Palladium Thiolate Bonding of Carbon Nanotube Thermal Interfaces," *Journal of Electronic Packaging*, Vol. 133, No. 2, 2011, pp. 020907-1–020907-6. doi:10.1115/1.4004094

[19] Panzer, M. A., Zhang, G., Mann, D., Hu, X., Pop, E., Dai, H., and Goodson, K. E., "Thermal Properties of Metal-Coated Vertically Aligned Single-Wall Nanotube Arrays," *Journal of Heat Transfer*, Vol. 130, No. 5, 2008, Paper 1052401. doi:10.1115/1.2885159

[20] Ngo, Q., Cruden, B. A., Cassell, A. M., Sims, G., Meyyappan, M., Li, J., and Yang, C. Y., "Thermal Interface Properties of Cu-Filled Vertically Aligned Carbon Nanofiber Arrays," *Nano Letters*, Vol. 4, No. 13, 2004, pp. 2403–2407. doi:10.1021/nl048506t

[21] Cross, R., Fisher, T. S., Xu, X., Gall, K., and Graham, S., "A Metallization and Bonding Approach for High Performance Carbon Nanotube Thermal Interface Materials," *Nanotechnology*, Vol. 21, No. 44, 2010, pp. 1–8. doi:10.1088/0957-4484/21/44/445705

[22] Gao, Z. L., Zhang, K., and Yuen, M. M. F., "Fabrication of Carbon Nanotube Thermal Interface Material on Aluminum Alloy Substrates with Low Pressure CVD," *Nanotechnology*, Vol. 22, No. 26, 2011, pp. 1–8. doi:10.1088/0957-4484/22/26/265611

[23] Zhang, Y., Xu, Y., Suhir, E., Gu, C., and Liu, X., "Compliance Properties Study of Carbon Nanofibres (CNFs) Array as Thermal Interface Material," *Journal of Applied Physics D: Applied Physics*, Vol. 41, No. 15, 2008, pp. 1–5. doi:10.1088/0022-3727/41/15/155105

[24] McNamara, A. J., Joshi, Y., and Zhang, Z. M., "Characterization of Nanostructured Thermal Interface Materials—A Review," *International Journal of Heat and Mass Transfer*," Vol. 62, No. S1, 2012, pp. 2–11. doi:10.1016/j.ijthermalsci.2011.10.014

[25] Lin, W., Shang, J., Gu, W., and Wong, C. P., "Parametric Study of Intrinsic Thermal Transport in Vertically Aligned Multi-Walled Carbon Nanotubes Using a Laser Flash Technique," *Carbon*, Vol. 50, No. 4, 2012, pp. 1591–1603. doi:10.1016/j.carbon.2011.11.038

[26] Cola, B. A., Xu, J., and Fisher, T. S., "Contact Mechanics and Thermal Conductance of Carbon Nanotube Array Interfaces," *International Journal of Heat and Mass Transfer*, Vol. 52, Nos. 15–16, 2009, pp. 3490–3503. doi:10.1016/j.ijheatmasstransfer.2009.03.011

[27] Raidongia, K., Jagadeesan, D., Upadhyay-Kahaly, M., Waghmare, U. V., Pati, S. K., Eswaramoorthy, M., and Rao, C. N. R., "Synthesis, Structure, and Properties of Homogenerous BC4N Nanotubes," *Journal of Materials Chemistry*, Vol. 18, No. 1, 2007, pp. 83–90. doi:10.1039/b712472d

[28] Gao, Y., Marconnet, A. M., Panzer, M. A., LeBlanc, S., Dogbe, S., Ezzahri, Y., Shakouri, A., and Goodson, K. E., "Nanostructured Interfaces for Thermoelectrics," *Journal of Electronic Materials*, Vol. 39, No. 9, 2010, pp. 1456–1462. doi:10.1007/s11664-010-1256-7

[29] Treacy, M. M. J., Ebbesen, T. W., and Gibson, J. M., "Exceptionally High Young's Modulus Observed for Individual Carbon Nanotubes," *Nature*, Vol. 381, No. 6584, 1996, pp. 678–680. doi:10.1038/381678a0

[30] Falvo, M. R., Clary, G. J., Taylor, R. M., Chi, V., Brooks, F. P., Washburn, S., and Superfine, R., "Bending and Buckling of Carbon Nanotubes Under Large Strain," *Nature*, Vol. 389, No. 6651, 1997, pp. 582–584. doi:10.1038/39282

[31] Won, Y., Gao, Y., Panzer, M. A., Dogbe, S., Pan, L., Kenny, T. W., and Goodson, K. E., "Mechanical Characterization of Aligned Multi-Walled Carbon Nanotube Films Using Microfabricated Resonators," *Carbon*, Vol. 50, No. 2, 2012, pp. 347–355. doi:10.1016/j.carbon.2011.08.009

[32] Maschmann, M. R., Amama, P. B., Goyal, A., Iqbal, Z., Gat, R., and Fisher, T. S., "Parametric Study of Synthesis Conditions in Plasma-Enhanced CVD of High-Quality Single-Walled Carbon Nanotubes," *Carbon*, Vol. 44, No. 1, 2006, pp. 10–18. doi:10.1016/j.carbon.2005.07.027

[33] Meyyappan, M., Delzeit, L., Cassell, A., and Hash, D., "Carbon Nanotube Growth by PECVD: A Review," *Plasma Sources Science and Technology*, Vol. 12, No. 2, 2003, pp. 205–216. doi:10.1088/0963-0252/12/2/312

[34] Vlasov, I. I., Ralchenko, V. G., Goovaerts, E., Saveliev, A. V., and Kanzyuba, M. V., "Bulk and Surface-Enhanced Raman Spectroscopy of Nitrogran-Doped Ultrananocrystalline Diamond Films," *Physica Status Solidi*, Vol. 203, No. 12, 2006, pp. 3028–3035. doi:10.1002/pssa.200671119

[35] Vlasov, I. I., Lebedev, O. I., Ralchenko, V. G., Goovaerts, E., Bertoni, G., Tendeloo, G. V., and Konov, V. I., "Hybrid Diamond-Graphite Nanowires Produced by Microwave Plasma Chemical Vapor Deposition," *Advanced Materials*, Vol. 19, No. 22, 2007, pp. 4058–4062. doi:10.1002/adma.200700442

[36] Huang, Z., Fisher, T., and Murthy, J., "An Atomistic Study of Thermal Conductance Across a Metal-Graphene Nanoribbon Interface," *Journal of Applied Physics*, Vol. 109, No. 1, 2011, pp. 426–430. doi:10.1063/1.3556454

[37] Vickerman, J. C., *Surface Analysis The Principal Techniques*, Wiley, West Sussex, England, U.K., 1977, pp. 135–152.

[38] Hu, H. P., Wang, X. W., and Xu, X. F., "Generalized Theory of the Photoacoustic Effect in a Multilayer Material," *Journal of Applied Physics*, Vol. 86, No. 7, 1999, pp. 3953–3958. doi:10.1063/1.371313

[39] Maschmann, M. R., Ehlert, G. J., Park, S. J., Mollenhauer, D., Maruyama, B., Hart, A. J., and Baur, J. W., "Visualizing Strain Evolution and Coordinated Buckling Within CNT Arrays by In Situ Digital Image Correlation," *Advanced Functional Materials*, Vol. 22, No. 22, 2012, pp. 4686–4695. doi:10.1002/adfm.201200676

[40] Yu, C., Saha, S., Zhou, J., and Shi, L., "Thermal Contact Resistance and Thermal Conductivity of a Carbon Nanofiber," *Journal of Heat Transfer*, Vol. 128, No. 3, 2006, pp. 234–237. doi:10.1115/1.2150833